Available online at www.sciencedirect.com
SCIENCE DIRECT®
Electrochimica Acta 50 (2005) 4426–4443
ELECTROCHIMICA Acta
www.elsevier.com/locate/electacta

Reaction and nucleation mechanisms of copper electrodeposition from ammoniacal solutions on vitreous carbon

Darko Grujicic, Batric Pesic *

University of Idaho, College of Engineering, Department of Materials Science and Engineering, McClure Hall, Moscow, ID 83844-3024, USA

Received 5 October 2004; received in revised form 26 December 2004; accepted 6 February 2005
Available online 13 March 2005

Abstract

The reaction and nucleation mechanisms of the electrodeposition of copper from ammoniacal solutions were investigated by cyclic voltammetric (cv) and chronoamperometric (ca) techniques, respectively. Each experiment with both electrochemical techniques was followed by morphological studies by atomic force microscopy (AFM). With respect to pH, the studies were performed on ammoniacal solutions at pH 4, pH 6, and pH 8, each representing a characteristic predominance region in *E*–pH diagrams. The experimental parameters were copper concentration, scanning rate, deposition potential, and electrode conditioning. It was found that at pH 4 copper electrodeposition occurs via reduction of cupric species to cuprous, which in turn can be either reduced, or disproportionated to metallic copper. At pH 6, deposition occurs from free and complexed cupric species, while at pH 8, only cupric amine complexes are involved. Copper nucleates according to instantaneous mechanisms at pH 4, and progressive nucleation mechanisms at pH 6 and pH 8. The diffusion coefficients of the copper species involved were also determined and are reported in this study.

Keywords: Copper–ammonia system; Copper nucleation; Atomic force microscopy; Scharifker–Hills nucleation models; Copper diffusion coefficients

1. Introduction

The electrodeposition of thin metal films is a viable alternative to vacuum-based deposition processes, such as sputtering, plasma deposition, or chemical vapor deposition [1,2]. Its major advantages are its simplicity, that processing can take place at room temperatures and pressures, and that thin film properties can be controlled. As the dimensions of copper structures continue to scale down into nanometer range, the initial stage of copper electroformation, i.e., nucleation, becomes increasingly important. Nucleation can be regarded as the most critical stage of growth for definition of the final film properties.

Copper nucleation mechanisms have been investigated on substrates such as vitreous carbon [3–5], sputtered TiN [6], and copper [7], from solutions containing sulfates [3], pyrophosphate [7], and fluoroborate [6]. Instantaneous copper nucleation mechanisms have been found in each of the cited studies, although inspection of electrode images from the fluoroborate solutions [6] also suggests progressive nucleation mechanisms. In addition, it was found [3] that the type of nucleation mechanism is highly dependent on the solution pH and the presence of a supporting electrolyte.

Among other chemical systems, those based on ammonia chemistry are of importance to copper electrodeposition because of the diverse speciation of aqueous cuprous and cupric ions. Only a few studies have been reported [8–10], however. Thus, Nila and Gonzales [8], in addition to their thermodynamic study of the Cu–NH_4Cl system, have found that copper deposition was controlled by the appearance of $Cu(OH)_2$ (at $pH \geq 11.85$) and a mixed precipitate $Cu(OH)_{1.5}Cl_{0.5}$ (at $4.62 \leq pH \leq 7.16$). No copper nucleation mechanisms were proposed. Ramos et al. [9] investigated the effect of chloride and nitrate anions on copper nucleation mechanisms. The very complex reaction mechanisms proposed involved re-dissolution of copper nuclei with nitrate ions. Theoretical models, although leaning toward progressive nucleation

* Corresponding author. Tel.: +1 208 885 6569; fax: +1 208 885 2855.
E-mail address: pesic@uidaho.edu (B. Pesic).

0013-4686/$ – see front matter © 2005 Elsevier Ltd. All rights reserved.
doi:10.1016/j.electacta.2005.02.012

mechanisms, remained inconclusive due to the lack of experimental verification of surface morphology. Graham et al. [10], on the basis of SEM morphological examination, confirmed the Volmer–Weber type of growth during electrodeposition of copper from Cu–NH_3 solutions onto TiN and copper substrates, but did not determine the nucleation mechanisms.

Due to the limited number of studies, the mechanisms of copper nucleation during electrodeposition from ammoniacal solutions have remained unclear. The aim of this work is to provide better understanding of the underlying mechanisms, utilizing the results from electrochemical (cv and ca) and morphological (AFM) studies.

2. Experimental

Solutions were prepared with reagent grade $CuSO_4$ and $(NH_4)_2SO_4$ and Type I purity water (Barnstead NANOpure II). The concentration of ammonium sulfate, which served as a buffering agent and a supporting electrolyte, was 1 M. Solution pH was adjusted by adding either dilute H_2SO_4 or NH_4OH.

The electrochemical setup was a standard three-electrode cell. The vitreous carbon working electrode (0.442 cm^2) was a non-porous disk (Sigri) with surface roughness close to 1 nm (root mean square) upon polishing with 0.05 μm-grade alumina. The reference electrode for cyclic voltammetric studies was a leak-free Ag/AgCl electrode ($E^0 = 0.222$ V versus NHE; Cypress Systems) and a copper wire (CuRE) immersed in a 0.05 M copper sulfate solution for nucleation studies. The difference between the redox potentials of the experimental solutions used in this study when measured with these two reference electrodes and converted to NHE was less than 15 mV. All potentials reported in this study are with respect to hydrogen electrode-NHE. Coiled copper wire served as a counter electrode. Electrochemical experiments were controlled by a potentiostat/galvanostat (AMETEK, PAR 273A), interfaced with a PC running PAR M270 software. Surface morphology was characterized by atomic force microscopy (AFM; VEECO, Digital Instruments, Model Nanoscope IIIa, MultiMode^{TM}) by imaging under fluid in taping mode. Statistical analysis of the AFM images for the purpose of calculating nuclei distributions, sizes and population densities was performed on several 15 μm × 15 μm and 5 μm × 5 μm images. The thermochemical software Stabcal [10] was used for thermodynamic calculations.

Speciation of Cu^+/Cu^{2+} ions in cathodic and anodic cv scans was probed by a scanning tunneling microscope (STM) modified for this research. Electrochemically, the setup was a four-electrode system consisting of: Working electrode-generator (glassy carbon), working electrode-collector (coated STM tip-Pt/Ir), counter electrode (gold) and reference electrode (leak-free Ag/AgCl). The STM piezo and controller were used merely for precise separation of the two working electrodes (20 μm). The electrochemical experiments were run by the external bi-potentiostat from CH Instruments (Model 760B).

3. Results and discussion

3.1. Copper–ammonia chemistry

A copper–ammonia phase diagram, calculated using the Stabcal program [11] in the form of *E*–pH, given in Fig. 1, has four characteristic pH regions. In the first region, between pH 0 and 4.8, cupric ion is the predominant soluble species.

The second region, pH 4.8–6.9, is characterized by copper present almost entirely in solid form; i.e., metallic copper, and cuprous and cupric oxides. Two aqueous cupric and one cuprous species are adjacent in extremely narrow fields. In the third region, pH 6.9–11.6, soluble copper is almost all represented by copper ammines, $Cu(NH_3)_4^{2+}$ and $Cu(NH_3)_2^{+}$.

Based on Fig. 1, pH 4, pH 6, and pH 8 were selected to represent three predominance regions. The fourth, pH 11.6–14, was not studied because of ammonia instability in this region.

3.2. Cyclic voltammetry coupled with morphological studies

Cyclic voltammetry (cv) studies performed at pH 4, 6, and 8 were followed by electrode surface morphology examination by AFM, to correlate the electrochemical data with the solid reaction products.

3.2.1. Cyclic voltammetry at pH 4

3.2.1.1. Effect of scanning rate. The effect of scanning rate on cyclic voltammetry at pH 4 is given in Fig. 2a. The voltammograms, all initiated at +800 mV, were scanned in the negative direction at rates ranging from 5 to 100 mV s^{-1}.

According to Fig. 2a, the cv's are characterized by two cathodic and two anodic peaks. The initial cathodic current

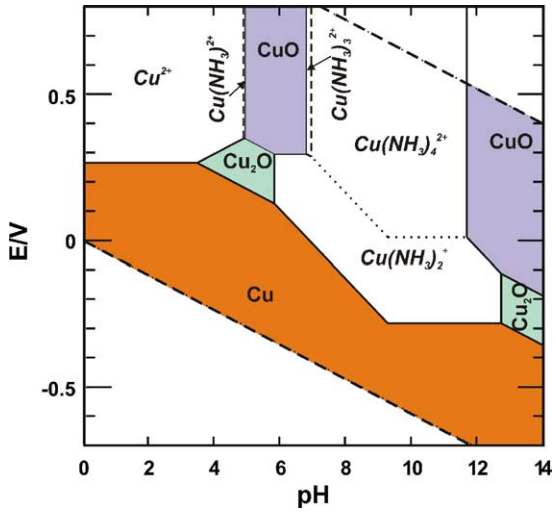

Fig. 1. E_{CuRE}–pH diagram of copper–ammonia system. Conditions: 0.005 M Cu^{2+}; 1.0 M $(NH_4)_2SO_4$.

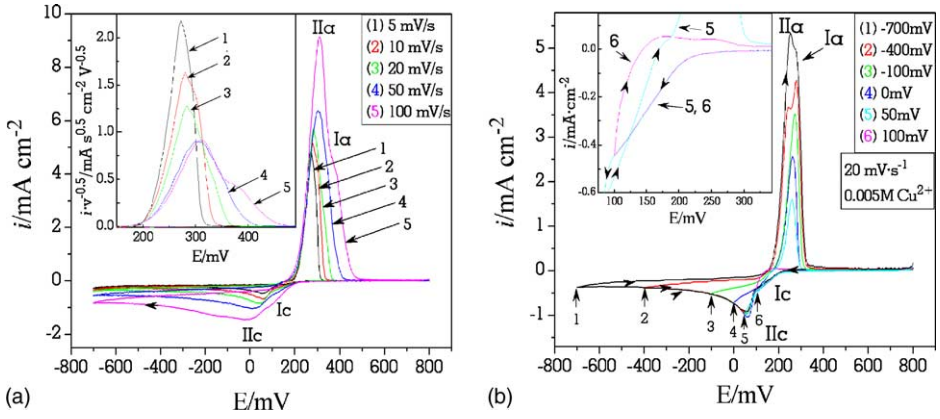

Fig. 2. Cyclic voltammetry of copper–ammonia system at pH 4 as function of: (a) scanning rate (inset: anodic peak currents normalized by the square root of scanning rate), and (b) vertex potential (inset: enlarged cv's 5 and 6). Each solution contained 1 M $(NH_4)_2SO_4$ as a supporting electrolyte.

increase, labeled Ic, was assigned to the reduction of cupric to cuprous ions, according to the following reaction:

$$Cu(H_2O)_6^{2+} + e = Cu(H_2O)_4^{+} \quad (1)$$

Reaction (1) is followed by disproportionation of the produced cuprous ions into metallic copper and cupric ions, reaction (2):

$$2Cu(H_2O)_4^{+} = Cu^0 + Cu(H_2O)_6^{2+} \quad (2)$$

At higher scanning rates, such as 100 mV s^{-1}, the initial current increase developed into a distinctive peak signifying dependence on diffusion to supply the cupric ions. The presence of metallic copper before the onset of peak IIc was confirmed in a separate AFM study (not presented here, a subject for a separate paper contribution).

Peak Ic was immediately followed by the second cathodic peak IIc, as the response to direct reduction of cupric ions (from the bulk and those from reaction (2)) to metallic copper, according to the following reaction:

$$Cu(H_2O)_6^{2+} + 2e = Cu^0 + 6H_2O \quad (3)$$

Characteristically, the onset of the reduction reaction (3) was more negative than its equilibrium potential, and was a function of scanning rate. Copper nucleation overpotential is a consequence of the nucleation work required to form copper nuclei of vitreous carbon [12], and the crystallographic misfit between the deposit and the substrate [13], considering that the surface of vitreous carbon consists of randomly oriented sp^2 carbon atoms, while copper atoms require ordered crystallization in face-centered cubic geometry.

Upon the sweep reversal at −700 mV, the current became anodic at about +200 mV. At slower scans, there was only one anodic peak, labeled IIa. This peak was not characterized by abrupt termination, which is typical for anodic dissolution of deposited metallic films [14]. Instead, the peak was almost symmetrical. Additionally, with the increase of the scanning rate, the peak labeled Ia appeared at first as a shoulder on the positive side of peak IIa, and then as a separate peak as the scanning rate increased (see the inset in Fig. 2a; normalized current with respect to the square root of scanning rate, according to Randles–Sevcik equation [15]). It is proposed that the first anodic reaction, peak IIa, is the oxidation of metallic copper to cupric ions, reaction (4):

$$Cu^0 + 6H_2O = Cu(H_2O)_6^{2+} + 2e \quad (4)$$

The appearance of the shoulder in the inset in Fig. 2a. suggests that subsequent to electrochemical reaction (4) the chemical reaction between the cupric ions accumulating on the surface and the remainder of metallic copper, reaction (5), occurs:

$$Cu^0 + Cu(H_2O)_6^{2+} = 2Cu(H_2O)_4^{+} + 2H_2O \quad (5)$$

The consideration that the second anodic peak could arise due to dissolution of copper nuclei of different sizes was ruled out after the in situ AFM study (not presented here) showed that copper disappears in unison. In a study of copper oxidation in ammonia solutions, Darchen et al. [16] have also concluded that oxidation of copper in ammoniacal solutions does not go through formation of Cu^+ but rather it proceeds directly to Cu^{2+}, which subsequently reacts with metallic copper to form Cu^+. As the potential sweep continues in the positive direction, Cu^+ formed through reaction (5) is further oxidized to Cu^{2+} according to reaction (6), corresponding to peak Ia:

$$Cu(H_2O)_4^{+} + 2H_2O = Cu(H_2O)_6^{2+} + e \quad (6)$$

At the end of peak Ia, the current decays to zero, indicating that all of the metallic copper from the surface is exhausted and that cuprous ions are oxidized to cupric.

In order to further verify the origins and existence of intermediary Cu^+ ion, related to reactions (2) and (5), a study based on the principles of scanning electrochemical microscopy [17] was conducted. The scanning tunneling microscope was used for precise separation between two working electrodes: the glassy carbon disk and the sharp STM tip. Conceptually, one electrode (glassy carbon) is used to generate (generator electrode) the species, by cyclic voltammetry, while the other electrode (STM tip) is used for their detection (collector electrode). The collector-tip electrode was positioned within the hydrodynamic layer of the generator-

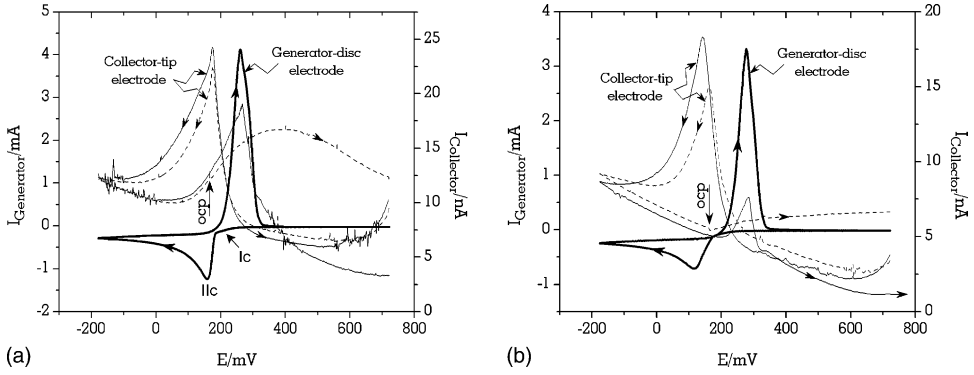

Fig. 3. Electrochemical microscopy detection of cuprous species formed during cyclic voltammetry in: (a) 0.01 M Cu^{2+} + 1 M $(NH_4)_2SO_4$ and (b) 0.01 M Cu^{2+} + 1 M Na_2SO_4 pH 4 solutions. The current traces recorded are: bold solid line, generator disk (glassy carbon) electrode; thin solid line, collector-tip electrode. Thin-dashed line represents the collector-tip currents when the glassy carbon generator-electrode was disconnected from the potentiostat at the potential labeled as OCP after reversing in anodic direction. Conditions: scanning rate, 20 mV s^{-1}. Generator electrode (glassy carbon) scanning range: +722 to −178 mV. Collector-tip electrode potential fixed at +722 mV.

disk electrode, less than 20 μm above its surface. By setting the potential of the collector-tip electrode under sufficiently positive potential, the arriving species would be oxidized if they were generated in the lower oxidation state on the opposite electrode. Here, the collector-tip electrode was held at +722 mV. It should be understood that in the present experimental system the only candidate species that could be oxidized on the collector-tip electrode are those from copper in cuprous form, if these were generated. Two sets of experiments were performed, the cyclic voltammetry from (a) ammoniacal, and (b) ammonia-free cupric sulfate solutions, Fig. 3a and b.

According to Fig. 3, the onset of the first cathodic peak Ic on the glassy carbon electrode is accompanied by the sharp increase of collector-tip current. Because the collector-tip current can only result from Cu^+ oxidation, it becomes conclusive that the cuprous ion species that arrived at the collector-tip electrode had to be produced at the glassy carbon generator-electrode, by reaction (1). As the potential on the glassy carbon electrode reached the values negative enough, the onset of peak IIc, to initiate the reduction of just produced cuprous ions, most of the cuprous ions would be consumed by reduction to metallic copper. Consequently, the current on the collector-tip electrode would sharply decrease, as was observed. The collector-tip current decreased up to the vertex potential, and continued to decrease when the scan was reversed into the positive direction, until about +60 mV, when it began to increase again. Because the current can only be produced by oxidation of Cu^+, and because the glassy carbon was still under reducing conditions when the increase of tip-current began, the ensuing conclusion is that the Cu^+ ions could only be produced by chemical stripping of metallic copper with Cu^{2+} present in solution, as stated in reaction (5). Further increase of the generator electrode potential in positive direction responded with a close correlation between the currents of the two electrodes. The increase of current on the glassy carbon electrode was caused by direct oxidation of metallic copper to Cu^{2+} by reaction (4). Just produced Cu^{2+} dissolved the underlying copper (chemical stripping) to produce Cu^+ ions by reaction (5), and these were detected on the collector-tip electrode by an adequate increase of current. When all of metallic copper was oxidized on the glassy carbon, the current sharply dropped, which was followed with a sharp drop of collector-tip current, as well.

Additional proof for generation of cuprous ions by chemical stripping, while sweeping in positive direction, came from the following experiment. The potential of glassy carbon electrode was swept in forward and reverse direction, except that upon reversal the glassy carbon electrode was disconnected from the potentiostat right before the onset of anodic current. In this experiment, the collector-tip current is represented by a dashed line; the generator-electrode current was reproducible and follows the same thick solid line up to the potential at which it was disconnected, marked as “OCP” in Fig. 3a and b. The expectation was that if Cu^+ ions were formed on the glassy carbon by electrooxidation of metallic copper then, upon disconnection from the potentiostat, the current of the collector-tip electrode should decline with the remaining duration of experiment because of the lack of further supply and oxidation of remnant Cu^+ at the tip-electrode. Opposite was observed, i.e., the collector-tip current kept increasing. The collector-tip current could only be sustained by continuous production of cuprous ions by chemical stripping, as given in reaction (5).

When the experiments were performed with ammonia-free solutions, i.e., with cupric sulfate in sodium sulfate solution as a supporting electrolyte, similar results were obtained, as shown in Fig. 3b. The importance of this experiment is to demonstrate that Cu^+ can be formed in pure sulfate solutions even in the absence of complexing agents. It should also be noticed that the current on the collector-tip electrode, upon disconnection of glassy carbon electrode, also increased with the remaining time but its magnitude was quite lower than the corresponding current from the ammonium sulfate solutions. This comparison clearly demonstrates much stronger

leaching power of Cu^{2+} when present in ammonium-based solutions.

The results of this study are in accordance with the results produced by Tindall and Bruckenstein [18–20], who were among the first to confirm formation of cuprous ions by chemical stripping, and more recently, by Vereecken et al. [21,22], where it was proven that electrooxidation of copper proceeds in one step, directly into Cu^{2+}. Because of its significance to electronic industry in the area of electroplating of copper interconnects, the chemistry of Cu^{2+}/Cu^{+}, alone and in the presence of Cu^{+} stabilizing agents, has been extensively studied, as recently reviewed by Vereecken et al. [22].

3.2.1.2. Effect of vertex potential. The proposed reactions for copper deposition and dissolution at pH 4 were further supported by examining the effect of reversal potential; i.e., the vertex potential, Fig. 2b. Setting the reversal potential to −400 mV resulted in a substantial decrease of peak IIa, which almost disappeared at vertex potentials −100 and 0 mV. The significance is that there was less metallic copper to oxidize when the forward reduction scan was reversed at more positive potentials, leaving Cu^{+} available for oxidation. A cyclic voltammogram reversed at 50 mV (inset) still had an anodic peak IIa, while the reversal at 100 mV recovered only peak Ia. Because there was no metallic copper involved, peak Ia has to correspond to the oxidation of Cu^{+} to Cu^{2+}. The vertex potential study simultaneously confirms that the first reduction step is the formation of cuprous ion, as Ia and Ic are related.

3.2.1.3. Effect of copper concentration. The effect of copper concentration was investigated for 0.001, 0.005, and 0.01 M Cu^{2+} solutions. Increased copper concentration increased the extent of the reactions, but had no effect on the reaction mechanisms. This parameter will not be discussed any further.

3.2.1.4. Surface morphology. The changes of electrode surface at various stages of cyclic voltammetry were determined by AFM study. Fig. 4 shows a cyclic voltammogram recorded at 20 mV s^{-1} in 0.005 M Cu^{2+} solution. Shaded overlays represent the calculated predominance areas of cupric and cuprous ions and metallic copper. The arrows indicate the positions at which a cv was stopped for AFM examination. The AFM images were taken in the ex situ mode.

At −100 mV, there were only a few large and small nuclei. The large nuclei probably correspond to copper initially formed by disproportionation of cuprous ions, while those smaller were the result of direct reduction of Cu^{2+}. Copper nucleation through disproportionation, prior to the peak Ic, was further confirmed by the in situ cv/AFM study (not presented here; to be published elsewhere). The second image, recorded at the vertex potential −700 mV, shows several large nuclei among numerous small nuclei, which were formed while scanning from −100 mV (peak IIc) to −700 mV, most likely by direct reduction to copper. After the cv reversal, at the very summit of the peak IIa, at +250 mV, the image shows that at this potential most of the small copper nuclei were already oxidized and removed by dissolution. Upon completion of scanning, at +800 mV, the electrode surface was barren, because anodic oxidation of Cu^{+} to Cu^{2+}, corresponding to peak Ia, left no solid oxidation products on the surface.

In order to examine the kinetics of copper nucleation in the reduction region of cyclic voltammetry, linear scanning voltammetry experiments were performed. Three scanning rates were selected (5, 20, and 100 mV s^{-1}) for one-directional scans from the initial potential +800 mV to the end potential E_v. The end potential was a variable in the range 0 to −700 mV, with a 100 mV increment. At the end of each scan, copper nuclei population density was measured by AFM. The resulting nuclei population densities are presented in Fig. 5.

According to Fig. 5, there are three distinct potential regions influencing nucleation. In the first potential range, from 0 to −100 mV, where copper nuclei are probably formed by disproportionation of cuprous ammine, population density was constant and independent of scanning rate (about 10^8 cm^{-2}). The second potential range began with the onset of direct copper reduction by reaction (3) at −100 mV, for all three scanning rates. This region was characterized by a steep increase in nuclei population density. The end of the second potential range was dependent on scanning rate, and shifted from −400 mV at 5 mV s^{-1} to −300 mV at 100 mV s^{-1}. The third potential range was characterized by a slow rate of increase in nuclei population density, almost independent of the scanning rate.

The slopes of linear fits through the second and third potential regions could be interpreted as the nucleation rates per millivolt, Table 1. Deceleration of the nucleation rate in the third potential region could be related to the saturation of the electrode surface with copper nuclei produced in the second potential region. Closer spacing of copper nuclei would cause the overlap of individual diffusion zones, decreasing the mass-transfer rate. Graham et al. [10] found a similar deceleration of the rate of nuclei cluster formation on the TiN surface, but explained it by the coalescence of individual nuclei.

3.2.2. Cyclic voltammetry at pH 6

3.2.2.1. Effect of scanning rate. The effect of scanning rate on cyclic voltammograms at pH 6 is given in Fig. 6a. The voltammograms, all initiated at +800 mV, were scanned in the negative direction at rates ranging from 5 to 100 mV s^{-1}. According to Fig. 6a, the cv's at pH 6 are characterized by three cathodic and two anodic peaks. The first cathodic peak, Ic, appeared at +200 mV, followed by the second cathodic peak, IIc, at +100 mV. The third cathodic peak, IIIc, appeared at about −500 mV.

The first cathodic peak Ic was assigned to reduction of cupric to cuprous ammine, according to reaction the following equation:

$$Cu(NH_3)_2^{2+} + e = Cu(NH_3)_2^{+} \quad (7)$$

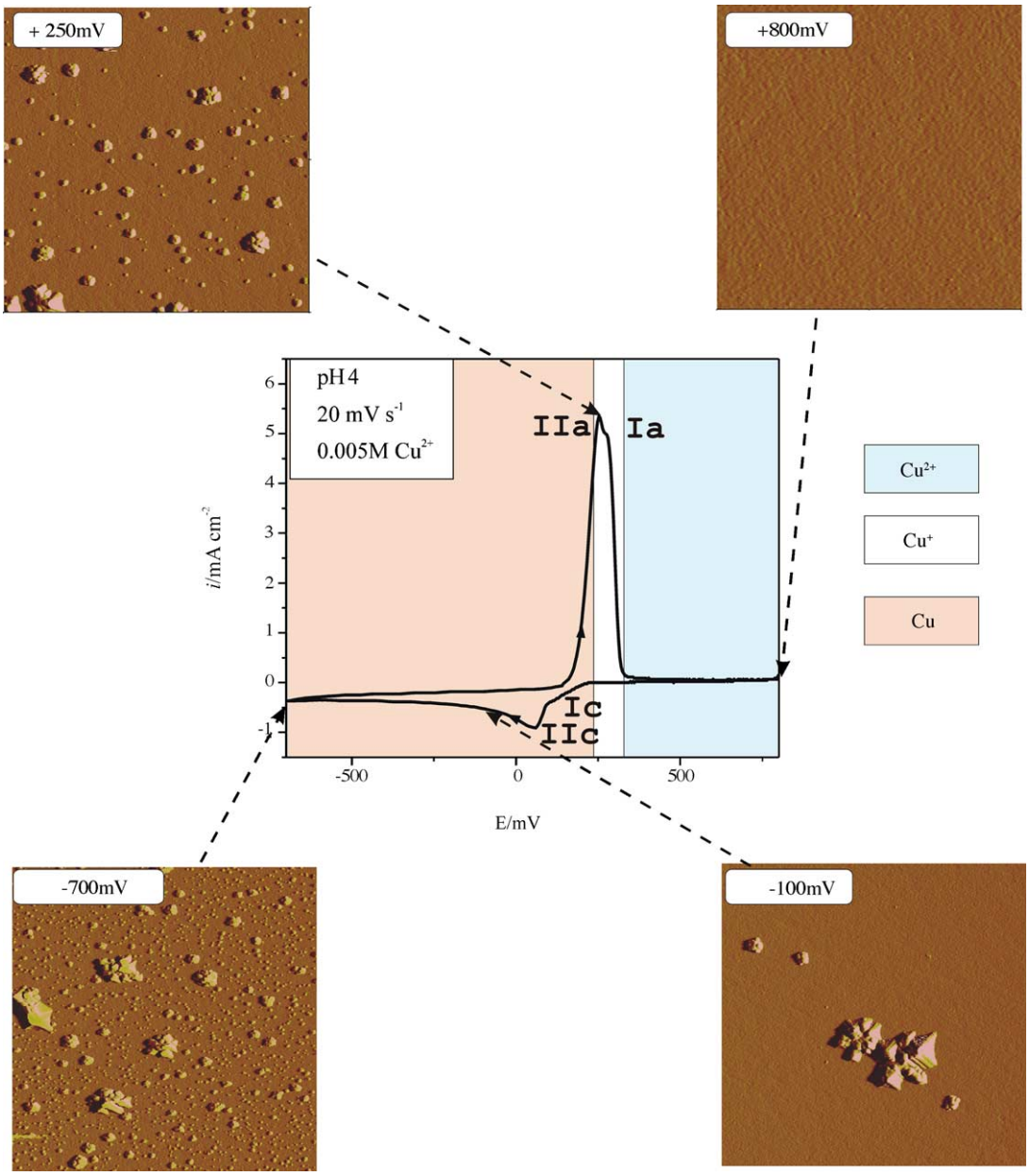

Fig. 4. Morphology of copper deposited in different stages of a cyclic voltammogram, at pH 4. Characteristic potentials noted in the AFM images are also indicated by the arrows. Shaded areas represent superimposed predominance regions for cupric ions, cuprous ions, and metallic copper. Conditions: 0.005 M $CuSO_4$ and 1 M $(NH_4)_2SO_4$, 20 mV s^{-1} scanning rate. AFM images are 5 μm × 5 μm.

Table 1
Nucleation population density as a function of the scanning rate and the end-potential used in the linear scanning voltammetry

Region	Scanning rate (mV s^{-1})		
	5	20	100
II	$\log N_0 = (5.7–5.8) \times 10^{-3} E_v$ ($E_v = -100$ to -400 mV)	$\log N_0 = (5.9–5.2) \times 10^{-3} E_v$ ($E_v = -100$ to -350 mV)	$\log N_0 = (6.4–3.8) \times 10^{-3} E_v$ ($E_v = -100$ to -300 mV)
III	$\log N_0 = (8.9–1.3) \times 10^{-3} E_v$ ($E_v = -400$ to -700 mV)	$\log N_0 = (8.3–1.4) \times 10^{-3} E_v$ ($E_v = -350$ to -700 mV)	$\log N_0 = (7.7–1.7) \times 10^{-3} E_v$ ($E_v = -300$ to -700 mV)

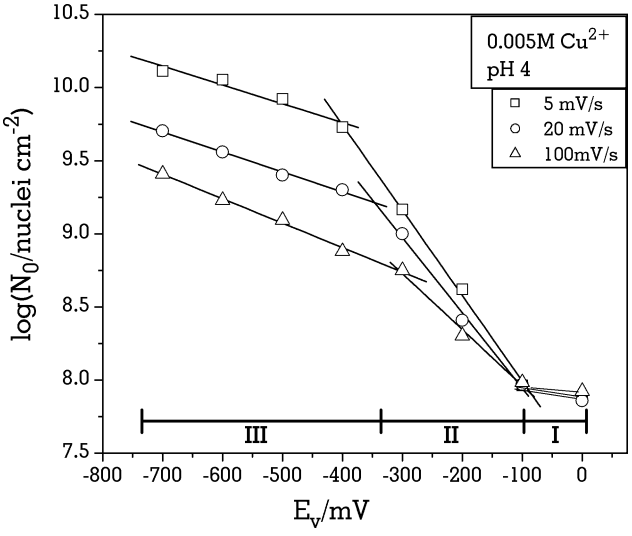

Fig. 5. Nuclei population density as a function of the scanning rate and the end-potential of linear scanning voltammetry. Nuclei population densities were measured by AFM.

Because of the low concentration of free ammonia at pH 6, the solution also contained free cupric ions, which were further reduced to metallic copper by reaction (3), resulting in the second cathodic peak, IIc.

Finally, the third cathodic peak IIIc represents the reduction of cuprous ammine, formed by reaction (7), to metallic copper, reaction (8):

$$Cu(NH_3)_2^{+} + e = Cu^0 + 2NH_3 \quad (8)$$

The scanning rate had an effect on the position of peaks. Thus, the peaks Ic and IIc shifted 45 and 30 mV, respectively, in a more negative direction with the increase of scanning rate from 5 to 100 mV s^{-1}. The peak IIIc shifted from −490 mV at 5 mV s^{-1} to −575 mV at 100 mV s^{-1}.

Upon sweep reversal, there were two anodic peaks. The first anodic peak, IIa, had onset at +170 mV, and its magnitude decreased with the increase of scanning rate. The increase of scanning rate was responsible for separation of the second anodic peak, Ia, which at slower scanning rates could only be recognized as a shoulder on the positive side of the peak IIa. In order to effectively separate the anodic peaks, the potential region +150 to +590 mV is presented in the inset of Fig. 6a, where the current density is normalized with respect to the square root of the scanning rate.

Like the reaction at pH 4, the proposed anodic reaction mechanism at pH 6 also consists of two electrochemical steps with an intermediate chemical reaction. Thus, the first anodic peak, IIa, corresponds to oxidation of metallic copper nuclei and simultaneous complexation with ammonia according to the following reaction:

$$Cu^0 + 2NH_3 = Cu(NH_3)_2^{2+} + 2e \quad (9)$$

Produced cupric amine reacts with the underlying metallic copper to form cuprous ammine, reaction (10)

$$Cu^0 + Cu(NH_3)_2^{2+} + 2NH_3 = 2Cu(NH_3)_2^{+} \quad (10)$$

Finally, the cuprous ammine is oxidized to cupric ammine (see reaction (7) in reverse order) producing anodic peak Ia. Note that at pH 6, the greater stability of the cuprous ammine complex causes a greater lag between peaks IIa and Ia than at pH 4, where the ammines are absent.

3.2.2.2. Effect of vertex potential. The effect of vertex potential on cv's at pH 6 is presented in Fig. 6b. The cyclic voltammogram reversed at −700 mV had a clearly defined anodic peak IIa and a shoulder corresponding to peak Ia. By setting the vertex potentials in the positive direction, the magnitude of IIa peak decreased. Thus, at the vertex potentials of −200 and 0 mV peak IIa was eliminated from the cv's altogether, leaving only peak Ia. The effect of vertex potential at pH 6 reveals similar underlying mechanisms as at pH 4, the only difference being the involvement of copper ammine species.

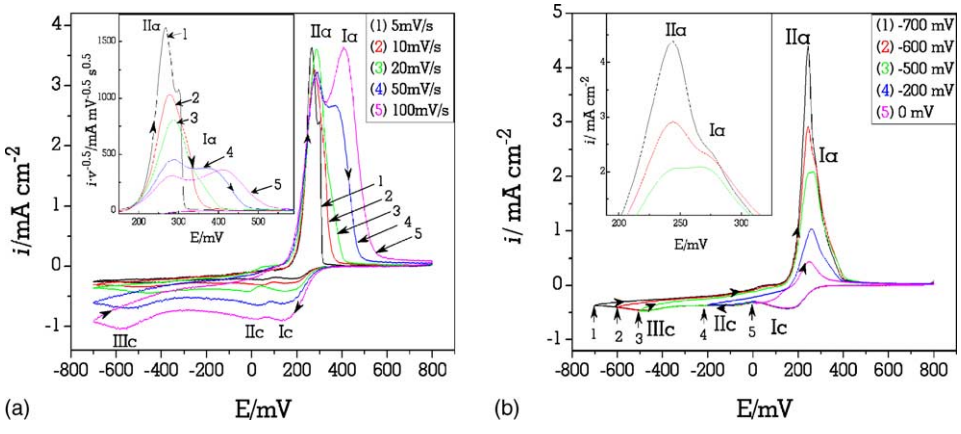

Fig. 6. Cyclic voltammetry of copper–ammonia system at pH 6 as a function of: (a) scanning rate and (b) vertex potential. The inset in (a) contains the anodic peak currents normalized by the square root of scanning rate. The inset in (b) shows the magnified region of anodic peaks. The effect of vertex potential was studied at 20 mV s^{-1} scanning rate.

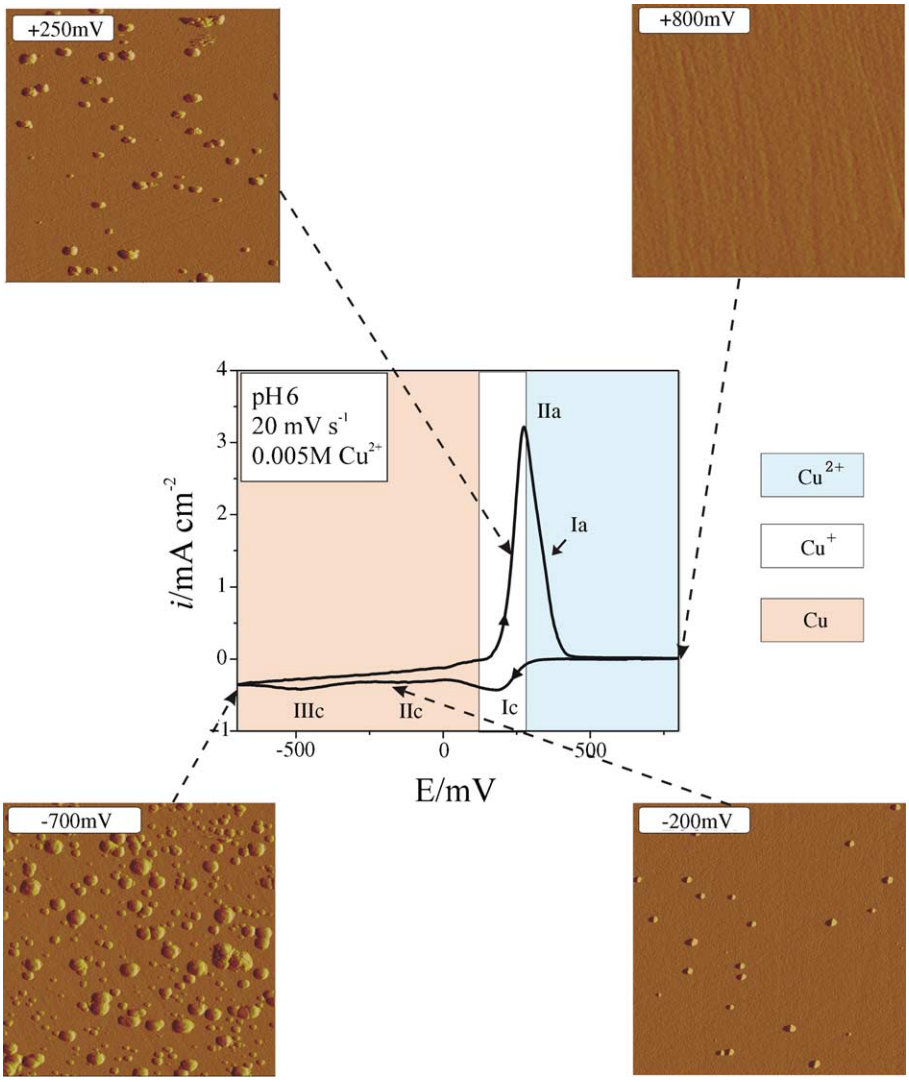

Fig. 7. Morphology of deposited copper in different stages of cyclic voltammetry at pH 6. Characteristic potentials are indicated by the arrows and noted in the corresponding AFM images. Shaded areas represent superimposed predominance regions for cupric and cuprous ions and metallic copper. Conditions: 0.005 M $CuSO_4$ and 1 M $(NH_4)_2SO_4$, 20 mV s^{-1} scanning rate. AFM images are 5 μm × 5 μm.

3.2.2.3. Surface morphology. Analogous to the study at pH 4, a morphological study of the electrode surface was performed at different stages of cyclic voltammetry at pH 6. A cyclic voltammogram, and the status of the electrode surface at four selected potentials, are presented in Fig. 7.

According to Fig. 7, the surface of vitreous carbon in the potential region beyond peak IIc was scarcely populated by uniformly sized copper nuclei. Compared to results at pH 4, there was a noticeable absence of large nuclei. The difference in the morphology of deposited copper at pH 4 and pH 6 coincides with the proposed deposition mechanisms. At pH 4, cuprous species are responsible for the occurrence of large nuclei by disproportionation, which is not the case at pH 6 where cuprous species are stabilized by free ammonia. The second image, taken at the vertex potential −700 mV, shows copper nuclei of various sizes, ranging from 30 to 350 nm in diameter. This type of morphology is characteristic for the progressive type of nucleation, characterized by continuous formation of new nuclei and their growth. The third image, taken during the sweep in the positive direction, at +250 mV, shows that the smaller nuclei had almost disappeared, while the larger were still on the surface. The population density at pH 6 was lower than the corresponding population density at pH 4. The image taken at +800 mV, the end of the cv scan, shows a barren surface, indicating the completion of electrodissolution of deposited copper.

3.2.3. Cyclic voltammetry at pH 8

3.2.3.1. Effect of scanning rate. The cyclic voltammograms at pH 8 are given in Fig. 8a. There were two cathodic and two anodic peaks, all distinct. The first cathodic peak, Ic, formed at +120 mV, represents the reduction of copper from cupric tetra-ammine complex, see Fig. 1, according to the following reaction

$$Cu(NH_3)_4^{2+} + e = Cu(NH_3)_2^{+} + 2NH_3 \quad (11)$$

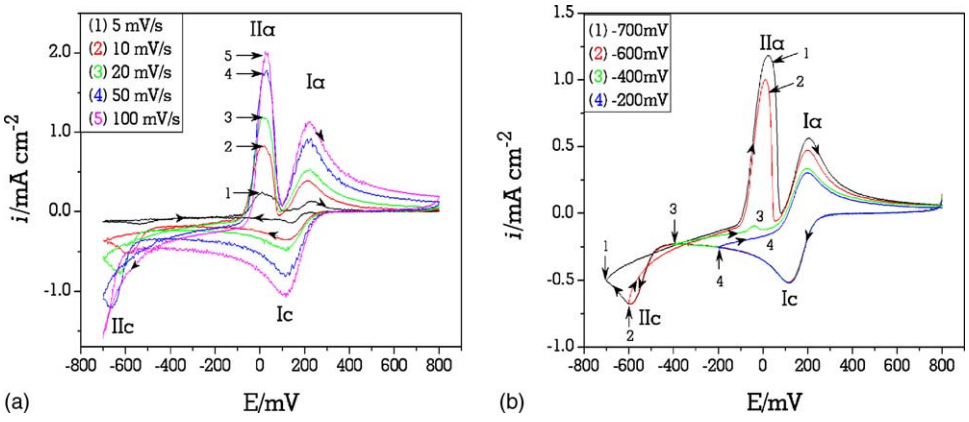

Fig. 8. Cyclic voltammetry of copper–ammonia system at pH 8 as a function of: (a) scanning rate, and (b) vertex potential. Solutions contained 1 M $(NH_4)_2SO_4$ as a supporting electrolyte. The scanning rate for cv's in Fig. 7b was 20 mV s^{-1}.

The position of peak Ia was independent of the scanning rate. The second cathodic peak, IIc, appeared close to the vertex potential of the cv, and was dependent on scanning rate. It shifted from −586 mV at 5 mV s^{-1} to −663 mV at 50 mV s^{-1}. At 100 mV s^{-1}, it was not fully defined. The dependence of its position on the scanning rate suggests the involvement of an electrodeposition reaction. Copper electrodeposition most likely proceeds initially through reaction (8), for which the reacting cuprous ammines species are formed by reaction (11). In the advanced stages, when cuprous ammine species are depleted, the reaction is sustained by direct reduction of bulk cupric ammine to metallic copper.

Upon the sweep reversal, the first anodic peak, IIa, appeared at +20 mV. The independence of the peak position from the scanning rate, and its very narrow and symmetrical shape, indicate that peak IIa corresponds to oxidation of metallic copper, reaction (12):

$$Cu^0 + 4NH_3 = Cu(NH_3)_4{}^{2+} + 2e \quad (12)$$

In the following step, the cupric species produced, which did not diffuse away from the copper surface, would oxidize metallic copper to the cuprous species produced, reaction (13):

$$Cu^0 + Cu(NH_3)_4{}^{2+} = 2Cu(NH_3)_2{}^{+} \quad (13)$$

The second anodic peak, Ia, appeared at +220 mV. Its position was not a function of scanning rate either, indicating a reversible process that includes soluble reactants and products. Peak Ia was therefore assigned to the oxidation of cuprous to cupric ammine, according to reaction (11).

3.2.3.2. Effect of vertex potential. The effect of vertex potential at pH 8 is presented in Fig. 8b. The first vertex potential at −700 mV represents the full cv cycle with two cathodic and two anodic peaks. Reversal of the cv scan at −600 mV decreased peak IIa, indicating a decreased amount of deposited copper. When the cv scan was limited to −400 mV (cv number 3), the voltage position before the onset of copper electrodeposition (peak IIc), a very small peak IIa (cv labeled with numeral 3) indicates that there was some metallic copper available for oxidation. Finally, the cv reversed at −200 mV contained only peaks Ic and Ia, the representatives of the reversible cupric/cuprous ammine couple, reaction (11).

There are two deposition mechanisms that could explain the presence of metallic copper above its bulk deposition potential; see the small peak IIa in the cv labeled with numeral 3 in Fig. 8b. These are the underpotential deposition and disproportionation mechanisms, of which the underpotential deposition of copper on vitreous carbon is a disputed mechanism. For example, Jaya et al. [23] found evidence for underpotential deposition on two types of vitreous carbon surfaces, contrary to findings by Danilov et al. [4]. Of the two most important parameters in the underpotential deposition: (1) the interaction energy and (2) the crystallographic misfit between the deposited atoms and the substrate [24], it is the second parameter which would not favor the underpotential deposition, as vitreous carbon resembles an entangled web of randomly distributed carbon microfibriles [25]. Additionally, the anodic peak was not preceded by a symmetrical cathodic peak, the most distinct experimental feature for the underpotential deposition [14]. Therefore, copper deposition above its deposition potential takes place by the disproportionation mechanisms.

3.2.3.3. Surface morphology. The morphology of the electrode surface in various stages of a cv cycle is presented in Fig. 9. Shaded areas, adopted from Fig. 1, represent superimposed stability regions of cupric and cuprous ion, and metallic copper.

The first image at −200 mV, the potential beyond the first cathodic peak Ic, shows a barren vitreous carbon surface, confirming that the reaction responsible for peak Ic, reaction (11), had no solid reaction products. The second image, taken at the vertex potential −700 mV, shows small copper nuclei, produced by the reduction of $Cu(NH_3)_2{}^{+}$ in reaction (8), represented by peak IIc. Due to a later onset of deposition, the nuclei produced were more uniform, and of smaller diameter,

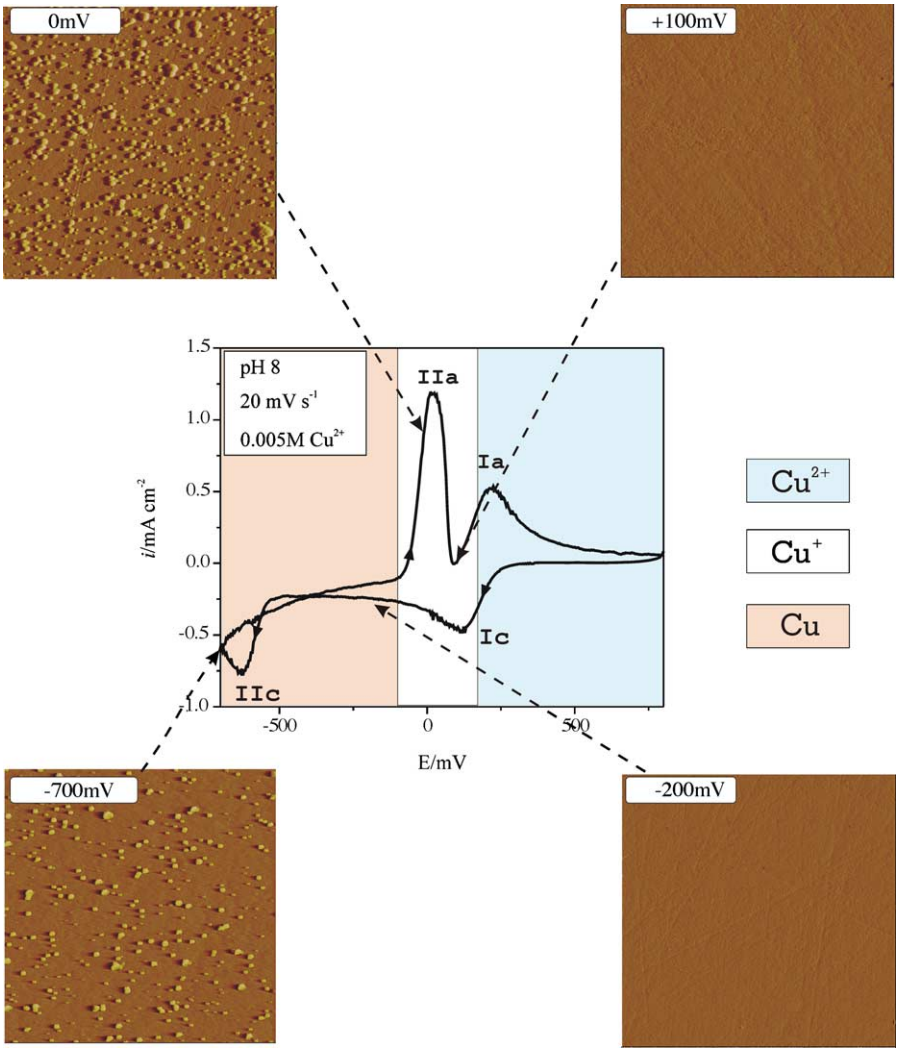

Fig. 9. Morphology of deposited copper in different stages of cyclic voltammetry at pH 8. Conditions: 0.005 M $CuSO_4$ and 1 M $(NH_4)_2SO_4$, 20 mV s^{-1} scanning rate. Note the excellent agreement between the thermodynamically calculated (shaded area) and the observed half-peak potentials Ic and Ia corresponding to the Cu^+/Cu^{2+} couple. AFM images are 5 μm × 5 μm.

than the corresponding nuclei at pH 4 and pH 6. The third AFM image, taken at 0 mV, on the more negative side of peak IIa, shows a densely populated surface with copper nuclei. However, the AFM image taken on the more positive side of the peak IIa; i.e., in the saddle between anodic peaks IIa and Ia, shows a barren surface. This image confirms the proposed mechanism that the first anodic peak, IIa, corresponds to the oxidation of metallic copper to cupric ammine, reaction (12), and that the second anodic peak, Ia, corresponds to the oxidation of cuprous to cupric ammine, reaction (11).

3.3. Chronoamperometry coupled with morphological study

Chronoamperometry (ca) was used to study the nucleation of copper mechanisms. In order to ensure the mass-transfer limitation, deposition potentials were selected from the corresponding cv's on the more negative side of cathodic peak IIc. In the absence of a nucleation process, the electrochemical equivalent of the potential step is represented by a current transient that persists until the steady-state mass-transport-controlled reaction is reached, as described by the Cottrell equation (14) [13]:

$$i(t) = \frac{nFD^{1/2}C_0}{\pi^{1/2}t^{1/2}} \tag{14}$$

where i is the current density, n the number of electrons involved, F the Faraday constant, D the diffusion coefficient, C_0 the concentration of species in the bulk, and t the time. For homogeneous reactions, current transient initially forms an abrupt signal and then promptly decays to the steady-state current. For heterogeneous reactions, nuclei formed on the surface contribute to the overall surface area by defining discrete diffusion zones that control the supply of reactants from the bulk of the solution. The resulting current transient deviates from the theoretical, described by Eq. (14), producing a

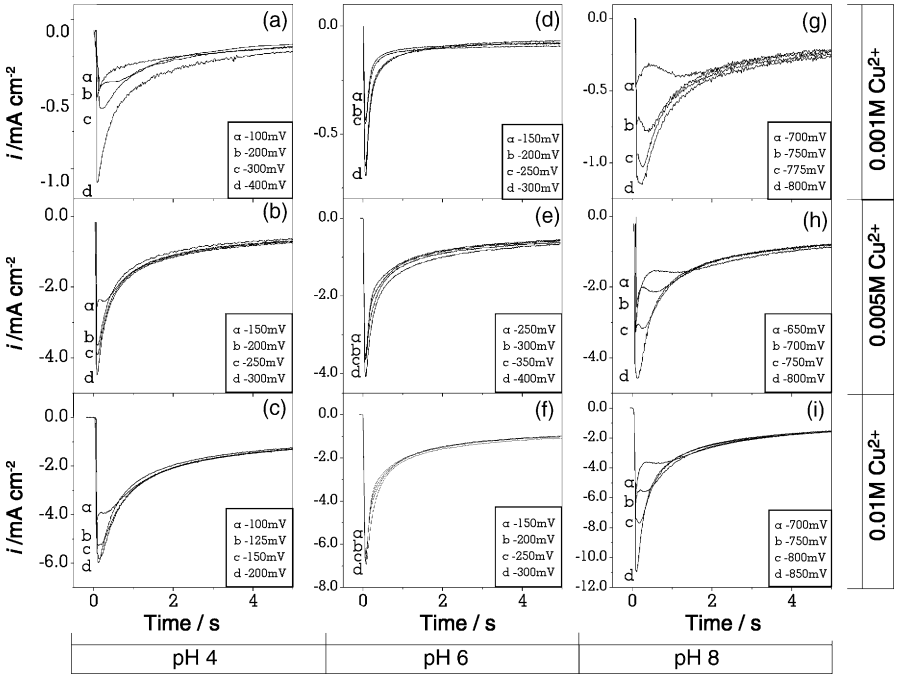

Fig. 10. (a)–(i) Chronoamperograms, recorded at different deposition potentials, as a function of solution pH and concentration of cupric ions.

peak instead of a sharp signal. When the individual diffusion zones eventually overlap, encompassing the entire electrode surface area, the reaction comes to a steady state as described by the Cottrell equation.

3.3.1. Chronoamperometry and nucleation modeling

The first five seconds of current transients recorded at pH 4, 6, and 8 for all three copper concentrations investigated are presented in Fig. 10a–i as lines a, b, c, and d, each corresponding to a different deposition potential. Each of the chronoamperograms in Fig. 10 was characterized by the initial current increase as a response to the applied potential, formation of a peak characteristic for nucleation, and final convergence to the limiting current corresponding to linear diffusion to a planar electrode, as described by Eq. (14).

There are several published methods that utilize the coordinates of chronoamperometric peaks to determine nucleation mechanisms and parameters related to nucleation (see the review article by Hyde and Compton [26]), among which the model developed by Scharifker and Hills [27] is the most widely used. This model allows simple and rapid classification of experimental transients into the two limiting nucleation mechanisms—instantaneous or progressive. Instantaneous nucleation, Eq. (15), corresponds to a slow growth of nuclei on a small number of active sites, all activated at the same time, while progressive nucleation, Eq. (16), corresponds to fast growth of nuclei on many active sites, activated during the course of electroreduction [28]:

$$\frac{i^2}{i_m^2} = \frac{1.9542}{\frac{t}{t_m}}\left\{1 - \exp\left[-1.2564\left(\frac{t}{t_m}\right)\right]\right\}^2 \quad (15)$$

$$\frac{i^2}{i_m^2} = \frac{1.2254}{\frac{t}{t_m}}\left\{1 - \exp\left[-2.3367\left(\frac{t}{t_m}\right)^2\right]\right\}^2 \quad (16)$$

where i_m and t_m are the current and the time, as respective peak coordinates. The plots of experimental current transients in $(i \cdot i_m^{-1})^2$ versus $t \cdot t_m^{-1}$ coordinates fall at either of these two limiting cases.

Fig. 11(a)–(i) shows the experimental current transients plotted in reduced current–time coordinates, along with the lines for instantaneous and progressive nucleation (solid and dashed lines, respectively), described by Eqs. (15) and (16).

According to Fig. 11a–c, the reduced current transients at pH 4 follow the instantaneous nucleation model for all three copper concentrations. At pH 6, the nucleation mechanisms switched to progressive nucleation, Fig. 11d–f. The nucleation mechanisms at pH 8 were also progressive, Fig. 11g–i, irrespective of copper concentration.

3.3.2. Morphological study of nucleation

3.3.2.1. Effect of copper concentration. The most useful method to validate the conformation of the nucleation mechanisms to the nucleation models was to conduct an AFM morphological study of the electrode after each chronoamperometric experiment. Fig. 12(a)–(i) presents the effect of solution pH on the morphology of deposited copper for the three copper concentrations investigated.

At the lowest copper concentration, 0.001 M, Fig. 12a–c, an increase in solution pH led to a decrease in nuclei population density, from 3×10^9 cm^{-2} at pH 4 to 3×10^8 cm^{-2} at pH 8. The mean diameter and the nuclei population density measurements should always be taken with caution, how-

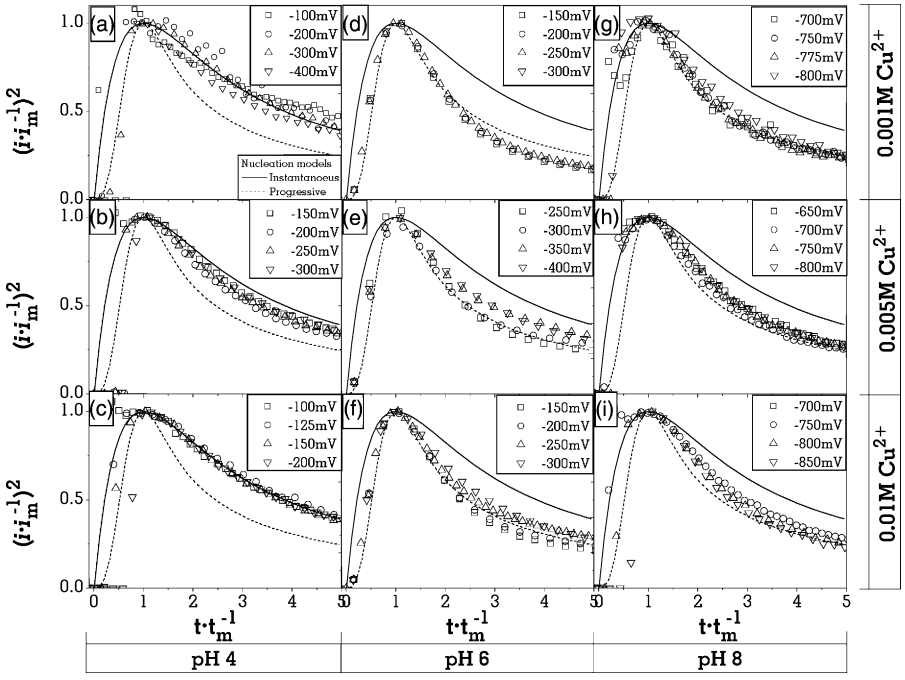

Fig. 11. (a)–(i) Reduced time vs. reduced current plots for chronoamperometric data in Fig. 9(a)–(i).

ever, because of non-uniform spreading of nuclei across the surface; i.e., the nuclei are often clustered.

When copper concentration increased to 0.005 M, Fig. 12d–f, an increase in solution pH had the opposite effect: the nuclei population density increased from 4×10^8 cm^{-2} at pH 4 to 2.7×10^9 cm^{-2} at pH 8. At the same time, mean nuclei diameter decreased from 200 nm at pH 4 to 90 nm at pH 8. The same effect, increase in nuclei population density and decrease of mean diameter, was also observed for the highest copper concentration, 0.01 M, Fig. 12g–i. Thus, the increase in solution pH from 4 to 8 increased the nuclei population density from 5×10^8 to 2.9×10^9 cm^{-2}. Mean nuclei diameter decreased from about 200 nm at pH 4 to about 85 nm at pH 8.

Regarding the nucleation mechanisms, the AFM study is essential as it can determine the mechanisms involved from the surface morphology. Thus, the uniform size distribution at pH 4 proves the instantaneous nucleation mechanisms. Conversely, the non-uniform size distribution at pH 6 and pH 8 proves the progressive nucleation mechanisms. In summary, the AFM morphological study should be regarded as the more precise approach for determination of nucleation mechanisms than the proposed mathematical models.

3.3.2.2. Effect of deposition potential. Fig. 13a–i presents the effect of deposition potential at pH 4, 6, and 8 in 0.005 M Cu^{2+} solutions. At pH 4, Fig. 13a–c, the nuclei population density increased from 3.33×10^8 cm^{-2} at −150 mV to 6.71×10^8 cm^{-2} at −250 mV, while their mean diameter decreased slightly from 173 nm at −150 mV to 161 nm at −250 mV. Deposition potential was more effective at pH 6 than at pH 4, Fig. 13d–f, with respect to both the nuclei size and population density. The nuclei population density increased from 2.85×10^8 cm^{-2} at −250 mV to 2.00×10^9 cm^{-2} at −350 mV, while the mean nuclei diameter decreased from 168 to 114 nm, respectively. At pH 8, Fig. 13g–i, the nuclei population density decreased from 3.35×10^9 cm^{-2} at −700 mV to 9.67×10^8 cm^{-2} at −800 mV, with a simultaneous increase in mean diameter from 84 to 115 nm.

3.3.2.3. Nuclei population density. For instantaneous nucleation mechanisms, the Scharifker–Hills model [27] can be used to calculate the nuclei population density from the peak coordinates (current density, i_m and corresponding peak time, t_m) on a current transient, Eq. (17):

$$N_0 = 0.065\left(\frac{1}{8\pi C_0 V_m}\right)^{1/2}\left(\frac{nFC_0}{i_m t_m}\right)^2 \tag{17}$$

where n is the number of electrons involved, F the Faraday constant, C_0 the concentration of species in the bulk, and V_m the molar volume.For progressive nucleation mechanisms, the model derived by Scharifker and Mostany [29] has to be used instead, Eq. (18):

$$i(t) = \frac{nFD^{1/2}C_0}{\pi^{1/2}t^{1/2}}\left\{1 - \exp\left[-N_0\pi k' D \times \left(t - \frac{1-\exp(-At)}{A}\right)\right]\right\} \tag{18}$$

where $k' = \frac{4}{3}\left(\frac{8\pi C_0 M}{\rho}\right)^{1/2}$, A the steady-state nucleation constant per site, and ρ the density of a deposited metal.

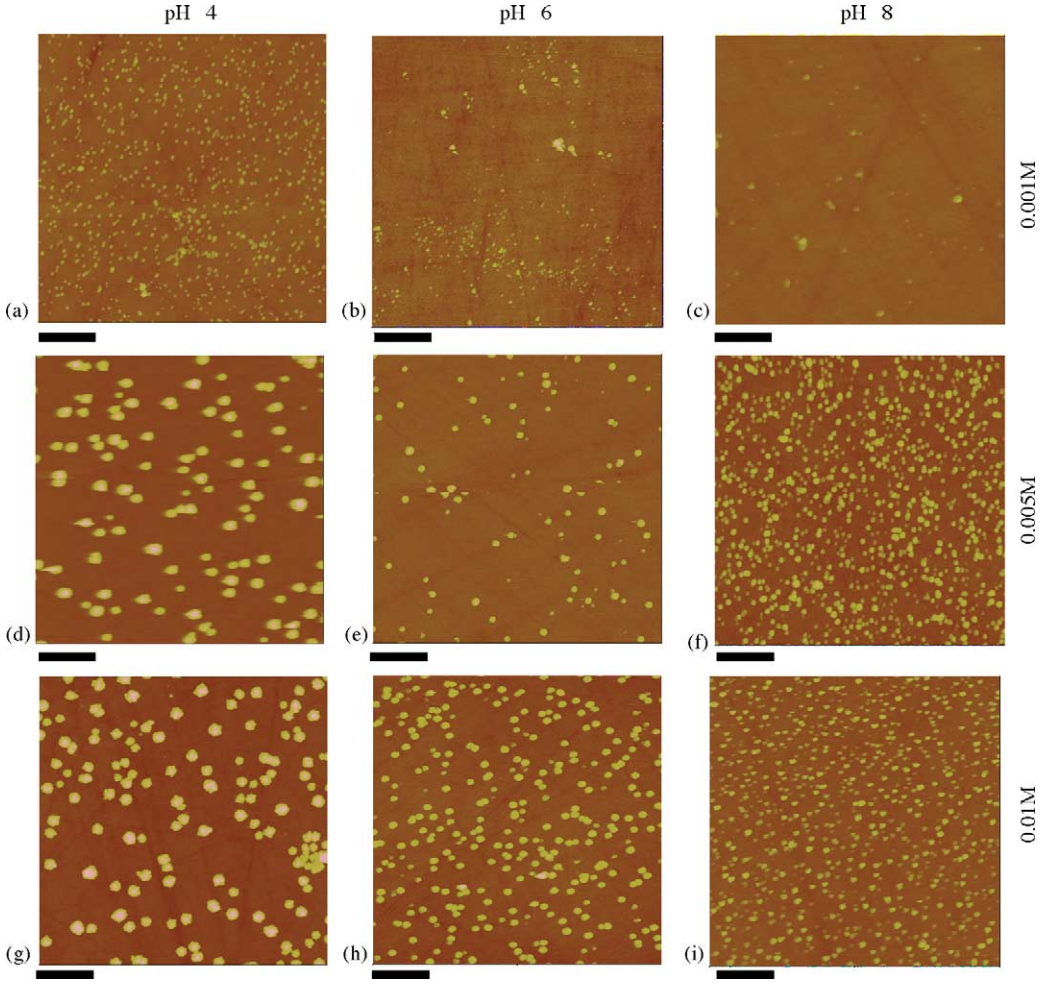

Fig. 12. (a)–(i) Effect of solution pH and copper concentration on morphology and nuclei population density. Conditions: respective deposition potentials, −200, −300, −800 mV for pH 4, pH 6 and pH 8; 1 M $(NH4)_2SO_4$ as a supporting electrolyte. AFM height mode: 200 nm vertical scale. Deposition time was 10 s. Scale bars: 1 μm.

Theoretical nuclei population densities, calculated from Eqs. (17) and (18), were compared to the nuclei population densities measured by Nanoscope AFM software and the estimations based on Faraday's law, which were obtained by dividing the total deposition current by the current required to deposit a single nucleus having a mean diameter, as estimated by AFM. The comparative study was performed on copper deposits from 0.005 M Cu^{2+} solutions at pH 4 and pH 8, Fig. 14.

At pH 4, the theoretical model given by Eq. (17) predicts the lowest nuclei population density for the deposition potential of −150 mV, and then a steady increase in the nuclei population density with an increasingly more negative potential. The actual nuclei population densities, measured by the Nanoscope software, were higher by about an order of magnitude than those predicted by the model, but followed the same trend. The nuclei population densities estimated from the total number of coulombs were of the same order of magnitude as those measured by the Nanoscope software, and almost independent of the deposition potentials.

At pH 8, the theoretical model given by Eq. (18) predicts an increase in nuclei population density with more negative deposition potentials. However, the actual nuclei population densities decreased as the deposition potential became more negative. Moreover, the measured nuclei population densities were one to three orders of magnitude higher than the model predictions. The estimations based on deposition charge were even higher, also following the decreasing trend.

Although the nuclei population density determination based on AFM measurements can have some problems while resolving the individual nuclei in a cluster of overlapping nuclei (images in Fig. 13g and h, for example), this method is still more accurate than the proposed mathematical equations. Deviation of the nuclei population density from the one predicted by the models has also been observed by other authors [7].

3.3.3. *Effect of electrode conditioning*

According to the results presented above, the change of solution conditions, such as pH, can change the nucleation

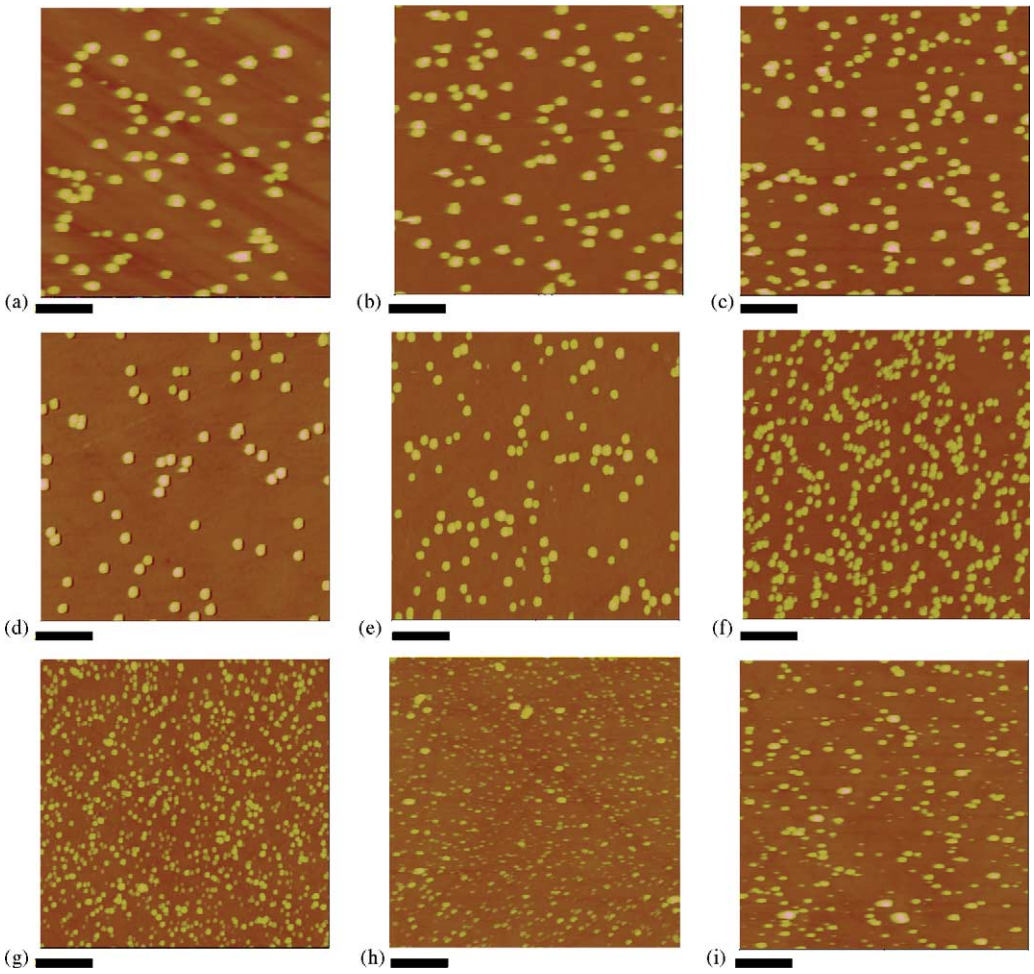

Fig. 13. (a)–(i) Effect of deposition potential and pH on morphology and nuclei population density. Deposition potentials at—pH 4: (a) −150 mV, (b) −200 mV, (c) −250 mV; pH 6: (d) −250 mV, (e) −300 mV, (f) −350 mV; and pH 8: (g) −700 mV, (h) −750 mV, (i) −800 mV. Conditions: deposition time 10 s; 0.0051 M Cu^{2+}; 1 M $(NH4)_2SO_4$. AFM height mode: 200 nm vertical scale. Scale bars: 1 μm.

mechanisms. In the copper–ammonia system studied, the mechanistic change is mainly the consequence of change of copper speciation with pH. However, the properties of the electrode surface can also have a significant effect on the mechanisms of the reactions involved. Two methods have been chosen to modify the surface of glassy carbon prior to electrodeposition. The methods are based on the effects of conditioning potential and conditioning time.

3.3.3.1. Effect of conditioning potential. The electrode was conditioned at various potential levels in two different electrolytes, 1 M $(NH_4)_2SO_4$, and 0.005 M Cu^{2+} + 1 M $(NH_4)_2SO_4$, each at pH 4 and pH 8. Conditioning in 1 M $(NH_4)_2SO_4$ was performed at potentials +1300, +800, −200, and −700 mV, using coiled Pt wire as a counter electrode and a leak-free Ag/AgCl reference electrode. Conditioning in copper–ammonia solutions at pH 4 was performed only at positive potentials, +1300 and +800 mV, to avoid copper deposition. For the same reason, conditioning in copper–ammonia solutions at pH 8 was performed at +1300, +800, and −200 mV. In all experiments, the conditioning lasted 120 s. After 120 s, the electrode was transferred wet to the electrodeposition cell containing 0.005 M Cu^{2+} + 1 M $(NH_4)_2SO_4$ of matching pH. Upon transfer, the potential was immediately stepped from the open circuit potential to −200 mV for pH 4, and to −800 mV for pH 8 solutions, for chronoamperometric deposition of copper for 10 s. The morphology of deposited copper was subsequently examined by AFM to measure the nuclei population density, in Fig. 15a, and the mean nuclei diameter, Fig. 15b.

At pH 4, according to Fig. 15a, the nuclei population density remained constant when the electrode was preconditioned at positive potentials. The presence of copper ions in the conditioning solution in this case was ineffective. However, the conditioning at negative potentials resulted in a sharp increase in population density of deposited nuclei, reaching about 5.9×10^9 cm^{-2} upon conditioning at −700 mV, which was equal to the nuclei population density under corresponding conditions at pH 8. At pH 8, the nuclei population density increased almost linearly with conditioning potential increasing in negative direction. The effect of conditioning potential on the nuclei population density can

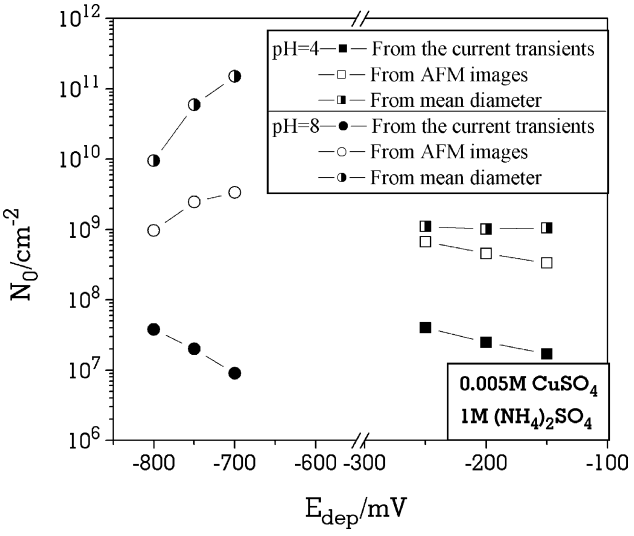

Fig. 14. Three comparative methods for copper nuclei population density estimation. The symbols represent: calculated values (full); values measured by AFM (open); and estimations based on deposition charge (semi-open). Electrodeposition performed from 0.005 M Cu solutions at pH 4 and pH 8, as a function of deposition potentials.

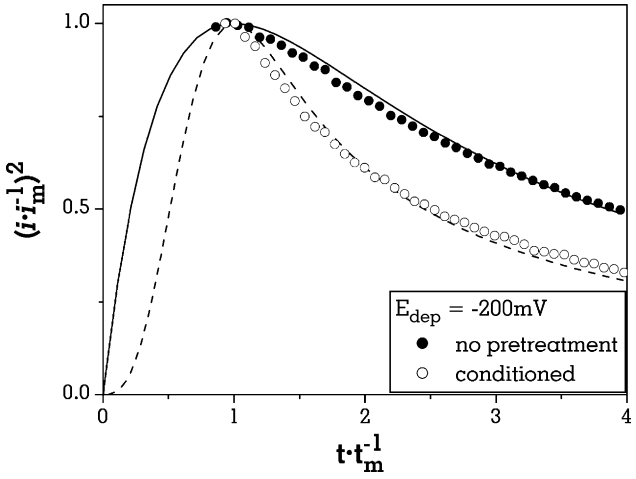

Fig. 16. Reduced current vs. reduced time plots of chronoamperograms recorded after deposition on freshly polished vitreous carbon electrode (full circles) and vitreous carbon that was pre-conditioned at −200 mV in 1 M $(NH_4)_2SO_4$ solution at pH 4 (open circles). Theoretical models for instantaneous and progressive nucleation mechanisms are shown as solid and dashed lines, respectively. Conditions: 0.005 M $CuSO_4$, 1 M $(NH_4)_2SO_4$, pH 4, deposition potential −200 mV.

also be expressed via the nuclei size: the smaller the size, the higher the population density. Fig. 15b clearly separates the role of conditioning potential in solutions with two different pH values.

Chronoamperograms for copper deposition with and without electrode pre-conditioning are presented in reduced current–time coordinates in Fig. 16, along with the Scharifker–Hills nucleation models for instantaneous and progressive nucleation, Eqs. (15) and (16).

According to Fig. 16, the chronoamperogram recorded at −200 mV with a freshly polished vitreous carbon electrode (closed circles) follows the instantaneous nucleation mechanism, as expected. On the other hand, a chronoamperogram recorded after the vitreous carbon electrode was conditioned for 2 min at −200 mV in a copper-free solution follows the progressive nucleation model. The change of nucleation mechanism is another indication that the properties of the vitreous carbon surface were affected by electrode conditioning.

It is very difficult to provide an explanation for the observed effects of potential conditioning of a glassy carbon electrode on the morphology and the mechanisms of copper deposition. The main source of difficulty is the complexity of the glassy carbon electrode surface with respect to its microstructure, the presence of surface oxides, which act as catalysts for electron transfer [30], and the unknown level of surface impurities. Most likely, any of these three parameters acts in combination with another. The effect of potential conditioning, which will require different research, cannot be explained here, but for now the focus will be placed on

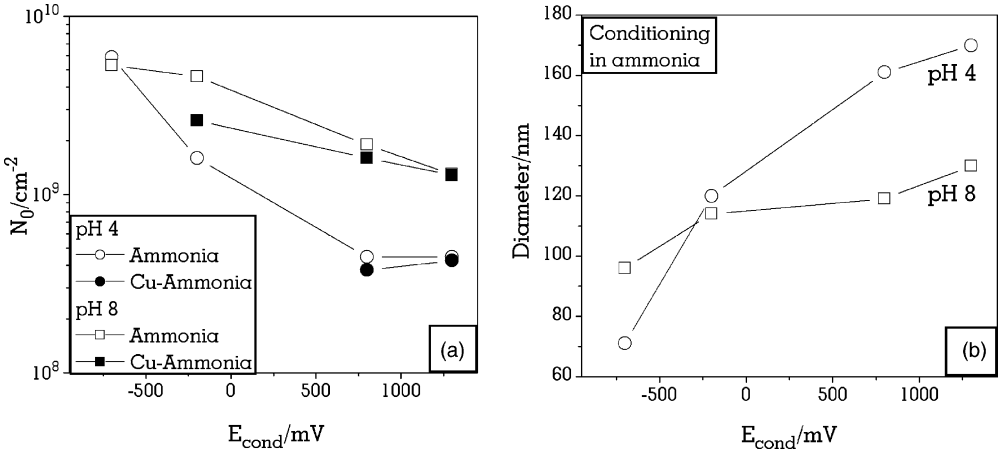

Fig. 15. (a) Effect of conditioning potential on nuclei population density as a function of solution pH and composition. (b) Dependence of a mean nuclei diameter on a conditioning potential.

the catalytic role of the carbonyl groups of glassy carbon. A typical polished GC surface has a 7–20% O/C ratio [31] with mostly carbonyl and hydroxyl functional groups. Most likely, the carbonyl groups are the most effective sites for electron transfer during electrodeposition of copper. Therefore, their number on the surface fixes the number of copper nucleation sites; i.e., nucleation follows instantaneous mechanisms. During the potential conditioning under reductive conditions, the catalytic carbonyl sites are blocked by some mechanisms, thus eliminating the possibility for instantaneous nucleation. Copper has to nucleate elsewhere on the surface as the sites become activated with time. These are the conditions for progressive nucleation mechanisms.

What is blocking the carbonyl sites remains to be explained. Some of the possibilities are the adsorption of NH_4^+ ions, the adsorption of hydrogen atoms, and the effect of localized pH increase. Localized pH increase, caused by removal of surface hydrogen ions, can be responsible for stabilization of ammonia on the same surface sites. Ammonia itself could cause the blockage of carbonyl groups.

3.3.3.2. Effect of conditioning time. Another parameter studied was the effect of conditioning time. The electrode was soaked under open circuit potentials in two different solutions, 1 M $(NH_4)_2SO_4$ and 1 M $(NH_4)_2SO_4$ + 0.005 M Cu^{2+}, each at pH 4 and pH 8. After soaking for 5, 120, and 600 s the electrode was transferred into a 0.005 M Cu^{2+} + 1 M $(NH_4)_2SO_4$ solution of the same pH as the conditioning solution for chronoamperometric deposition. The ca deposition lasted 10 s, and the potentials were −200 mV at pH 4, and −800 mV at pH 8.

The examination of the surface by AFM revealed that the conditioning time was not an effective parameter.

3.4. Calculation of diffusion coefficients

3.4.1. Diffusion coefficients based on cyclic voltammetry

Diffusion coefficients, which consider diffusion of soluble species without and with formation of an insoluble product, can be calculated from Randles–Sevcik [13] equations (19) and (20), respectively.

$$i_p = -(2.69 \times 10^5) n^{3/2} C_0 D^{0.5} v^{0.5} \quad (19)$$

$$i_p = -(3.67 \times 10^5) n^{3/2} C_0 D^{0.5} v^{0.5} \quad (20)$$

where i_p is the peak current density in A cm^{-2}, C_0 the concentration of species in the bulk of solution in mol cm^{-3}, D the diffusion coefficient in cm^2 s^{-1}, and v the scanning rate in V s^{-1}. Accordingly, the diffusion coefficients of soluble species, determined from the slopes of i_p versus $v^{0.5}$ plots, are given in Table 2.

The results in Table 2 show that the diffusion coefficients of cupric species increase as pH increases. The observed effect of pH can be explained by considering the coordination chemistry of cupric ions. A cupric ion in aqueous solution is coordinated by six water molecules, $Cu(H_2O)_6^{2+}$, in its primary hydration shell, followed by water molecules in the secondary and the tertiary hydration shells. In the primary shell, four water molecules are situated in the equatorial positions and two in the axial positions of an octahedron, the center of which is occupied by the cupric ion. Berces et al. [32] calculated that the four equatorial water molecules have the highest binding energies. Addition of ammonia to the aqueous solutions leads to formation of copper-amino complexes by successive replacement of water with ammonia ligands [33]. Due to the preference of Cu^{2+} ion for nitrogen over oxygen coordination [32], water molecules in the equatorial positions become replaced with ammonia molecules. Thus, at pH 4 all of the positions in the primary hydration shell are occupied by water molecules, while at pH 8 four water molecules have been replaced by the ammonia ligands, which also weaken the bonds with the secondary and tertiary hydration shells. Therefore, the mobility of cupric ions; i.e., their diffusion coefficients, is affected by pH, and increases as pH increases.

Table 2
Diffusion coefficients calculated from cyclic voltammograms according to Eqs. (19) and (20)

pH	Species	$10^5 D$ (cm^2 s^{-1})		
		0.001 M	0.005 M	0.01 M
4	Cu^{2+}	0.60×10^{-5}	0.37×10^{-5}	0.32×10^{-5}
6	$Cu(NH_3)_2^{2+}$	0.86×10^{-5}	0.44×10^{-5}	0.37×10^{-5}
6	$Cu(NH_3)_2^{+}$	1.18×10^{-5}	0.28×10^{-5}	0.34×10^{-5}
8	$Cu(NH_3)_4^{2+}$	2.09×10^{-5}	0.60×10^{-5}	0.59×10^{-5}
8	$Cu(NH_3)_2^{+}$	2.68×10^{-5}	0.77×10^{-5}	0.64×10^{-5}

Peaks used for calculations are: at pH 4 peak IIc (Fig. 2a), at pH 6 peaks Ic and IIIc (Fig. 5a) and at pH 8 peaks Ic and IIc (Fig. 7a).

With regard to the copper–ammonia system, there are no data available in the literature for comparison. The diffusion coefficients of cupric ion found in the literature are: 6×10^{-6} cm^2 s^{-1} for cupric ions in carbonate solutions, buffered with H_3BO_3 and HBF_4 [5]; 7×10^{-6} cm^2 s^{-1} for cupric ions in a nitrate solution [34], and 5.7×10^{-6} cm^2 s^{-1} for cupric ions in a hydroxide complex [34].

Coordination of cuprous ion in aqueous solutions is tetrahedral [33], so the primary hydration shell contains four water molecules, only two of which can be replaced with the ammonia ligands. Therefore, the diffusion coefficients of cuprous ammines are higher in comparison to those of cupric ammines. The addition of ammonia has the same effects as those discussed above for cupric ions.

3.4.2. Diffusion coefficients based on chronoamperometry

According to the Cottrell equation (14), the diffusion coefficients of reacting species can be determined from a slope of chronoamperograms in i versus $t^{-0.5}$ coordinates. Since the initial part of the current transient deviates from the Cottrell equation because of the nucleation processes, linearization can be performed only after the reduction reactions become limited by planar diffusion; i.e., beyond the peak stage of chronoamperograms. The results are

Table 3
Copper diffusion coefficients calculated from chronoamperograms according to the Cottrell equation (14)

$[Cu^{2+}]$ (M)	$10^5 D$ ($cm^2\ s^{-1}$)		
	pH = 4	pH = 6	pH = 8
0.001	1.37	1.99	2.71
0.005	0.77	1.02	1.5
0.01	0.65	0.94	1.4

presented in Table 3. Although there is some difference from the results based on cyclic voltammetry, the trend regarding the effects of pH and concentration remains the same. It should also be noted that the negative effect of an increase in copper concentration is the result of a decrease in the ratio of free ammonia to copper, which affects the mobility of copper species as discussed above.

4. Conclusions

Copper electrodeposition and electrodissolution were studied by using cyclic voltammetry and chronoamperometry. Each electrochemical experiment was followed by morphological examination by AFM. The following conclusions can be made.

1. The mechanisms of the involved reactions are a function of pH because of the effect this parameter has on copper speciation. At pH 4, copper speciates as the aquo complexes of cupric ions, as a mixture of the aquo and the amino complexes at pH 6, and as a mixture of amino complexes at pH 8.
2. During electrodeposition at pH 4, cupric ions are at first reduced to cuprous ions, which are in turn reduced to metallic copper. At pH 6, copper deposition takes place from the mixture of aquo and amino complexes in two different potential regions. At pH 8, metallic copper forms on the surface before the onset of bulk deposition. The mechanism responsible for formation of metallic copper is probably disproportionation of cuprous ammines into metallic copper and cupric ammines. Copper formed by disproportionation is confirmed by AFM.
3. At pH 4, copper nucleates according to instantaneous mechanisms. Progressive nucleation mechanisms govern copper nucleation at pH 6 and pH 8.
4. Copper concentration is not an effective parameter for the mechanisms of the redox reactions involved.
5. Conditioning of the electrode at more cathodic potentials affects the nucleation mechanisms at pH 4, but not at pH 8. Thus, at pH 4, the switch from instantaneous to progressive nucleation is most likely caused by the blockage of carbonyl groups as the most preferential sites for electron transfer. Which species are involved in the blockage, and whether the proposed blockage is the correct cause remain unknown, warranting further research for a definite answer.
6. Diffusion coefficients were calculated for each copper concentration and solution pH studied. It was found that mobility of both cupric and cuprous ions is affected by the coordination in the first hydration shell (ammine versus aquo ligands). Consequently, diffusion rates increased as pH increased, and decreased as copper concentration increased.

Acknowledgements

This work was sponsored by the U.S. Department of Defense, Department of the Navy, Office of Naval Research, Grant Number N000140110829; and The National Science Foundation RII Award (EPS 0132626).

References

[1] J.W. Dini, in: M. Schlesinger, M. Paunovic (Eds.), Modern Electroplating, 4th ed., Wiley, New York, NY, 2000.
[2] P.C. Andricacos, C. Uzoh, J.O. Dukovic, J. Horkans, H. Deligianni, IBM J. Res. Dev. 42 (5) (1998) 567.
[3] D. Grujicic, B. Pesic, Electrochim. Acta 47 (2002) 2901.
[4] A.I. Danilov, E.B. Molodokina, Yu.M. Polukarov, Russ. J. Electrochem. 38 (7) (2002) 732.
[5] A.I. Danilov, E.B. Molodokina, A.A. Baitov, I.V. Pobelov, Yu.M. Polukarov, Russ. J. Electrochem. 38 (7) (2002) 836.
[6] G. Oskam, P.M. Vereecken, P.C. Searson, J. Electrochem. Soc. 146 (4) (1999) 1436.
[7] A. Radisic, J.G. Long, P.M. Hoffmann, P.C. Searson, J. Electrochem. Soc. 148 (1) (2001) C41.
[8] C. Nila, I. Gonzales, J. Electroanal. Chem. 401 (1996) 171.
[9] A. Ramos, M.M. Hernandez, I. Gonzales, J. Electrochem. Soc. 148 (4) (2001) C315.
[10] L. Graham, C. Steinbruchel, D.J. Duquette, J. Electrochem. Soc. 149 (8) (2002) C390.
[11] H.-H. Huang, STABCAL—stability calculation for aqueous systems, Montana Tech of the University of Montana, Butte, MT.
[12] A. Milchev, Electrocrystallization: Fundamentals of Nucleation and Growth, Kluwer Academic Publishers, Boston, 2002.
[13] Southampton Electrochemistry Group, in: T.J. Kemp (Ed.), Instrumental Methods in Electrochemistry, Ellis Horwood Ltd., Chichester, UK, 1985.
[14] M. Noel, K.I. Vasu, Cyclic Voltammetry and the Frontiers of Electrochemistry, Oxford & IBH Publishing Co., New Delhi, India, 1990.
[15] A.J. Bard, L.R. Faulkner, Electrochemical Methods, Fundamentals and Applications, 2nd ed., Wiley, New York, NY, 2001, p. 512.
[16] A. Darchen, R. Drissi-Daoudi, A. Irzho, J. Appl. Electrochem. 27 (1997) 448.
[17] A.J. Bard, M.V. Mirkin (Eds.), Scanning Electrochemical Microscopy, Marcel Dekker, 2001, ISBN: 0-8247-0471-1.
[18] G.W. Tindall, S. Bruckenstein, Anal. Chem. 40 (1968) 1402.
[19] G.W. Tindall, S. Bruckenstein, Anal. Chem. 40 (1968) 1051.
[20] G.W. Tindall, S. Bruckenstein, Anal. Chem. 40 (1968) 1637.
[21] P.M. Vereecken, F.V. Kerchove, W.P. Gomes, Electrochim. Acta 41 (1996) 95.
[22] P.M. Vereecken, R.A. Binstead, H. Deligianni, P.C. Andricacos, IBM J. Res. Dev. 49 (2005) 3.
[23] S. Jaya, T.P. Rao, G.P. Rao, Electrochim. Acta 31 (1986) 343.
[24] S. Vinzelberg, G. Staikov, W. Lorenz, The Electrochemical Society Proceedings, vol. 94-31, 1994, p. 1.

[25] K. Kinoshita, Carbon, Electrochemical and Physicochemical Properties, Wiley, New York, NY, 1988.
[26] M.E. Hyde, R.G. Compton, J. Electronal. Chem. 549 (2003) 1.
[27] B. Scharifker, G. Hills, Electrochim. Acta 28 (7) (1983) 879.
[28] M.P. Pardave, M.T. Ramirez, I. Gonzales, A. Serruya, B.R. Scharifker, J. Electrochem. Soc. 143 (5) (1996) 1551.
[29] B. Scharifker, J. Mostany, J. Electroanal. Chem. 177 (1984) 13.
[30] P. Chen, M.A. Fryling, R.L. McCreery, Anal. Chem. 67 (1995) 3115.
[31] P. Chen, R.L. McCreery, Anal. Chem. 68 (1996) 3958.
[32] A. Berces, T. Nukada, P. Margl, T. Ziegler, J. Phys. Chem. A 103 (1999) 9693.
[33] A. Cotton, G. Wilkinson, Advanced Inorganic Chemistry, 3rd ed., Wiley, New York, 1972.
[34] E. Norkus, J. Appl. Electrochem. 30 (2000) 1163.